THE JOURNAL OF PHYSICAL CHEMISTRY C
A JOURNAL OF THE AMERICAN CHEMICAL SOCIETY

pubs.acs.org/JPCC

Article

Infrared Near-Field Spectroscopy of Gold Nanotriangle Fabry-Pérot Resonances

Published as part of The Journal of Physical Chemistry C virtual special issue "Honoring Michael R. Berman".

Vishal Kumar, Andrew W. Rossi, Zachary R. Lawson, Robert D. Neal, Jordan A. Hachtel, Svetlana Neretina, David J. Masiello,* and Jon P. Camden*

Cite This: *J. Phys. Chem. C* 2023, 127, 6777−6784

Read Online

ACCESS | Metrics & More | Article Recommendations | Supporting Information

ABSTRACT: In this work, we characterize the near-field response of individual gold nanotriangles over a broad, visible-to-infrared, spectral region (200−1500 meV) using high-resolution electron energy-loss spectroscopy (EELS) performed inside of a scanning transmission electron microscope (STEM). We begin by experimentally imaging the spatial and spectral extent of each nanotriangle's plasmonic Fabry-Pérot modes and measuring the evolution of their resonance energies with increasing edge length; thereby providing detailed information on infrared plasmon dephasing times and dispersion relations. Numerical electromagnetic simulations of the electron probe are used to interpret these experimental results and to compare the near-field electromagnetic enhancement factors of gold nanotriangles and nanorods of equal resonant energy. Taken together, this combined experimental and theoretical study provides unique insights relevant to designing noble metal plasmonic nanoparticle systems for solar energy harvesting and sensing applications in the near- and mid-infrared.

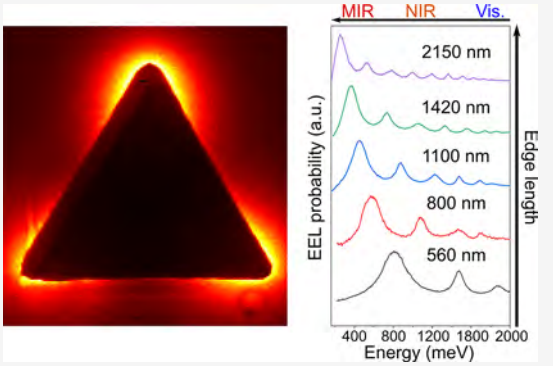

1. INTRODUCTION

Noble metal nanostructures have emerged as powerful optical tools owing to their ability to efficiently confine long wavelength electromagnetic radiation to nanometer length scales.[1,2] This ability to confine electromagnetic radiation has been widely exploited in the visible and near-infrared (NIR) regions to develop efficient solar energy harvesting, sensing, and catalytic applications.[3−5] Recently, there has been increased interest in extending plasmonic responses to the mid-IR (∼50−500 meV) region,[6,7] as it encompasses molecular vibrations[8] and phonons of solid-state materials.[9,10] Careful studies of the near-field responses of IR plasmonic materials will aid the development of new physical and chemical platforms capable of targeted analyte detection schemes,[11] surface-enhanced spectroscopies,[12] harnessing IR Fano interferences,[13] and strategies for efficiently capturing and manipulating IR solar[7] and thermal[14] radiation at the nanoscale.

Noble metal nanowires have received significant interest as they host high quality dipolar and higher-order multipolar plasmonic Fabry-Pérot modes,[15−17] which can be tuned by changing their aspect ratio to span the broad IR spectral window between 50−1000 meV. Past studies focusing on visible plasmon resonances have revealed that sharp-faceted nanostructures such as cubes, triangles, and other polygons exhibit higher near-field enhancement factors leading to stronger light-matter interactions.[18−20] Among these, triangle-shaped noble-metal nanostructures have received prominent interest[21] owing to their highly tunable plasmonic responses,[22] strong electromagnetic near-fields,[23] tridirectional polarization-dependent scattering,[24] nonlinear optical properties,[25] and ability to sustain strong plasmon-exciton polaritons.[26] However, a direct comparison between high aspect ratio nanstructures such as nanowires[15−17] and nanotriangles[22−24] has been lacking, especially in the IR region even though such comparisons would aid the design of plasmonic systems capable of efficiently manipulating IR radiation at the nanoscale. Although numerous studies explore the colloidal synthesis of plasmonic nanowires;[16,27,28] the synthesis of uniform-thickness gold nanotriangles (NTs) has proven difficult. This is especially true for the longer edge-length nanostructures sustaining plasmons in the IR, owing to their three-dimensional expansion which inhibits growth in the

Received: February 2, 2023
Revised: March 14, 2023
Published: March 30, 2023

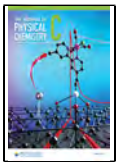

https://doi.org/10.1021/acs.jpcc.3c00753
J. Phys. Chem. C 2023, 127, 6777−6784

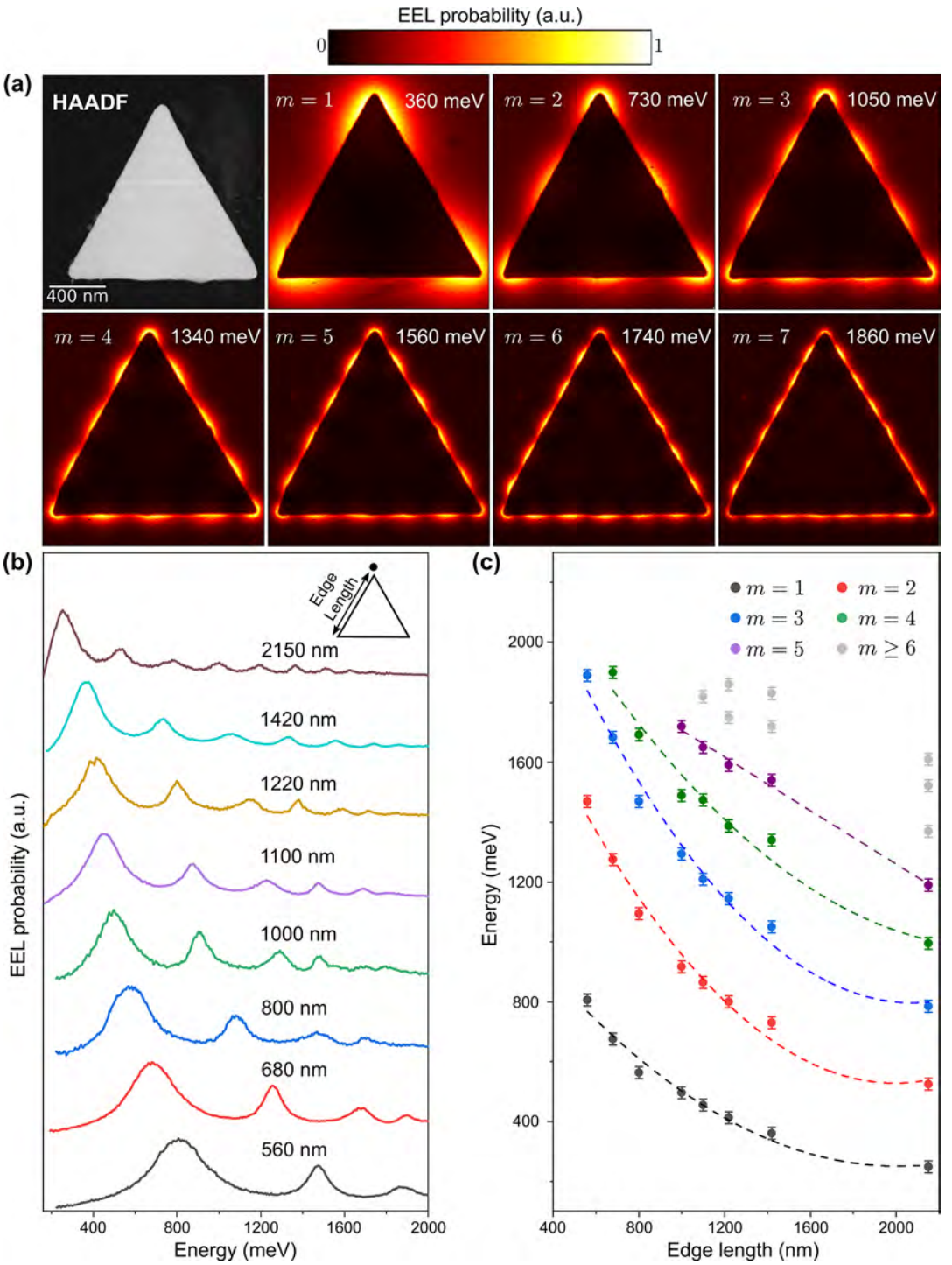

Figure 1. (a) Representative EEL spectrum images for a 1420 nm gold NT displaying the spatial profiles of its m = 1−7 FP modes and (b) EEL spectra of a set of individual gold NTs versus edge length. Each point spectrum is acquired at the NT tip. (c) Dependence of the resonance energy of different NT FP modes versus NT edge length.

lateral directions.[29] Alternatively, electron-beam lithography can synthesize gold NTs of desired edge lengths[30] but this method significantly increases the cost. To circumvent this problem, we recently devised a new approach for the colloidal synthesis of uniform thickness and controllable edge-length gold NTs directly on substrates[31] and here we employ this synthetic method to study the near-field responses of NTs throughout the visible-to-IR spectral region.

Conventional far-field optical spectroscopies have diffraction-limited spatial resolution and are subjected to optical selection rules, thus limiting the study of the near-field response properties of plasmonic nanostructures.[32−34] Scanning near-field optical microscopy (SNOM) can overcome the diffraction limit by exploiting the properties of evanescent waves but is limited by weak light sources and poor detectors in the IR (∼1−10 μm).[35,36] Alternatively, electron-energy loss spectroscopy (EELS) performed in a scanning transmission

https://doi.org/10.1021/acs.jpcc.3c00753
J. Phys. Chem. C 2023, 127, 6777−6784

electron microscope (STEM) can map the near-field responses of plasmonic nanostructures at high-spatial resolution (~1 nm) across a broad spectral window in a single scan.[37,38] The evanescent waves associated with a fast traveling electron beam excite all plasmon modes, dipolar and nondipolar, allowing for the spectral- and spatial-mapping of both bright and dark plasmon modes.[39,40] Additionally, recent advancements in monochromators and direct-electron detectors now allow access to low-energy IR excitations with a high signal-to-noise ratio, enabling vibrational spectroscopy with high spatial resolution.[41−45]

In this study, we combine our new synthesis strategy with electron beam characterization and theoretical simulations to investigate the near-field IR response of gold NTs. Specifically, we map the dipolar and higher order multipolar plasmonic FP modes of a set of NTs with 560−2150 nm edge lengths at high spatial (~1 nm) and spectral (~16 meV) resolution using monochromated STEM-EELS. The dependence of the plasmonic FP resonance energies and spectral line widths on the NT edge length is explored from 200−1500 meV. Companion numerical electrodynamics simulations using an electron probe are used to interpret these results and to additionally compare the near-field electromagnetic enhancement factors for gold NTs with high aspect ratio gold nanowires. Our results suggest that sharply faceted gold NTs can concentrate IR radiation and provide valuable insights for optimizing nanostructure shapes to efficiently harness energy from the visible to IR spectral regions.

2. METHODS

2.1. Materials. SiN_x TEM grids with a membrane thickness of 20 nm were sourced from SIMPore Precision Membrane Technologies. Sputter deposition targets of Au and Sb were cut from a 0.5 mm thick foil (99.9985% purity, Alfa Aesar) and 19 mm diameter rod (ESPI Metals), respectively. The Au seed self-assembly process was carried out in ultrahigh purity Ar (Airgas). The liquid-phase NT synthesis utilized hydrogen tetrachloroaurate (HAuCl4, 99.99% trace metal basis, Beantown Chemical), hexadecyltrimethylammonium bromide (CTAB, >99% purity, Millipore Sigma), Brij-700 block copolymer (average MW 4,670, Spectrum Chemicals), and deionized (DI) water (18.2 MΩ·cm).

2.2. Gold NT Synthesis. The Au NT synthesis was adapted from a prior study demonstrating the formation of substrate-immobilized nanotriangles in periodic arrays on (0001)-oriented Al_2O_3.[31] The overall process yields single-crystal Au seeds formed in periodic arrays[46] after which they are subjected to a liquid-phase synthesis that transforms them into Au NTs. Here, adaptations were made to accommodate the use of SiN_x TEM grids as the substrate material. Insulating SiN_x grids were used to avoid additional quenching mechanisms influencing plasmon line widths.[47] Au seeds are prepared using a vapor-phase self-assembly process in which continuous layers of Sb (20 nm) and Au (0.4 nm) are sequentially sputter-deposited onto a SiN_x grid and then twice temperature cycled from room temperature to 1010 °C over a 25 min duration in a tube furnace under an Ar gas flow. Sb, which is sacrificial, was lost to the vapor phase but where its inclusion in the assembly process largely determines the spacing between the Au nanoparticles.[48] The liquid-state NT synthesis proceeds by placing the SiN_x grid at the bottom of a Parafilm-capped 30 mL beaker to which DI water (9 mL), Brij-700 (2 mL, 30 mM), and CTAB (1.5 mL, 10 mM) are added. The solution was then heated to 37 °C and magnetically stirred at 150 rpm. After 20 min, the reaction was initiated by adding $HAuCl_4$ (1.2 mL, 10 mM) and allowed to proceed for 8 h. The reaction was terminated by removing the grid from the growth solution and gently rinsing it with ethanol.

2.3. STEM-EELS Measurements. Low-loss STEM-EELS measurements were performed using an aberration-corrected and monochromated high-energy resolution STEM-EELS (Nion MAC STEM) located at Oak Ridge National Laboratory (ORNL).[49] The instrument was operated at an accelerating voltage of 60 kV with a convergence angle of 30 mrad and a collection angle of 25 mrad. The beam current was ~10 pA, and the scattered electrons were dispersed in a Nion Iris spectrometer at a 5.25 meV dispersion per channel. The energy resolution of the EEL spectra was measured by calculating the full-width half-maximum (fwhm) of the zero-loss peak (ZLP), which yields an energy resolution of 16−21 meV for the measurements reported here. All EEL images were acquired at an acquisition time of 30 ms and aligned and normalized with respect to the ZLP. The EEL spectrum profiles are obtained by averaging over an area of 25 × 25 nm^2 for smaller and 50 × 50 nm^2 for larger gold NTs near the tip of gold NT from the corresponding spectrum images. The local thickness of synthesized nanostructures was measured using the EELS log-ratio method,[50] and gold NTs of similar thickness were chosen for our study (Figure S1). Plasmon line width analysis was done by fitting the EELS profiles with Lorenztian peaks.

2.4. Numerical Simulation. All simulations were performed using the metallic nanoparticle boundary element method (MNPBEM) toolbox[51] with a background refractive index of unity in the absence of a substrate. The NTs were modeled using dielectric data for gold taken from Raschke and co-workers.[52] For all simulations, the electron acceleration voltage and beam waist were 60 kV and 0.2 nm, respectively. To compute the plasmon dephasing times of the $m = 1$ mode shown in the inset of Figure 2b, line widths were extracted by fitting the simulated EEL spectra displayed in the Supporting Information with Lorentzian functions. In Figure 3, the electron beam impact parameter was raster scanned with a step size of 5 nm.

3. RESULTS AND DISCUSSION

Figure 1 displays EEL spectra and spectrum images of a collection of single crystal gold NTs of varying edge lengths. Each spectral resonance and spatial mode profile corresponds to a specific Fabry-Pérot (FP) edge mode of an individual gold NT. FP modes arise from the constructive interference of counter-propagating surface plasmon polariton waves[53] and depend only on the nanostructure edge length rather than upon the nanostructure's general symmetry. As with nanowires,[22] constructive interference is realized when an integer number of half surface plasmon wavelengths fits along a nanostructure edge, yielding multiple resonant modes determined by $kL = m\pi - \phi$. Here, $k = 2\pi/\lambda$ and λ are the surface plasmon polariton wavenumber and wavelength, L is the NT edge length, m is the FP mode number, and ϕ is the phase shift accumulated upon reflection at the NT boundaries. The near-field response of each FP mode is probed at high spatial (~1 nm) and energy (~16 meV) resolution using monochromated STEM-EELS. Recent technological advancements, most importantly direct-electron detectors,[54] enable the

https://doi.org/10.1021/acs.jpcc.3c00753
J. Phys. Chem. C 2023, 127, 6777−6784

efficient imaging of multiple plasmonic FP modes which were previously limited by low signal-to-noise ratios.

The high-angle annular dark-field (HAADF) and corresponding EEL spectrum images in Figure 1a show the spatial profiles of the m = 1−7 FP modes of a single 1420 nm edge-length NT. The nodes and antinodes of each mode are clearly discernible without the use of any data filtering or smoothing processes. Also, the spatially resolved spectrum images show that the lower-order FP modes (m = 1,2) have a greater spatial extent of the EEL probability as compared to higher FP modes (e.g., m = 6,7), which can be explained by the increased spill-out of the NT's surface plasmon polaritons into the surrounding dielectric medium at lower frequencies.[17,55] Numerical EEL simulations (Figures S2−S3) demonstrate good agreement with these spectrum images. Additional experimental EEL spectrum images for other NT edge lengths are shown in Figures S4−S5.

Figure 1b displays a collection of EEL spectra each obtained near the tip of a series of NTs of varying edge lengths, showing a progressive red-shift in resonance energy with an increasing edge length. Notably, the dipolar (m = 1) resonance energies red shift and their linewidths decrease as the edge length increases from 560 to 2150 nm. The observed EEL spectra agree well with simulations, which also show narrower plasmonic line widths for longer gold NTs (Figure S6). The spectral positions of the m = 1−7 NT FP modes versus edge length are collected in Figure 1c. Similar to the m = 1 mode, the higher-order multipolar modes also red-shift with an increasing edge length. Also, we observed that the resonance energies red-shift nonlinearly with an increasing NT edge length.

Figure 2a shows the energy-momentum dispersion of the m = 1−7 FP modes collected from the set of NTs displayed in Figure 1. We observe that the FP resonances approach the light line ($\omega = kc$) with decreasing plasmon energy or an increasing edge length. With increasing plasmon energy (for all modes m), the dispersion curve red-shifts significantly from the light line. The observed convergence to the light line can be explained by the fact that the FP modes become less confined to the NT's gold interior at lower energies and larger edge lengths.[55] We additionally analyze the plasmon line widths by fitting the experimental FP resonance peaks with a Lorentzian profile (Figure S7).[56] We observe that the full width at the half-maximum (fwhm) decreases with an increasing edge length (Figure S8), while the associated plasmon dephasing time, used to quantify the quality of a mode, increases with an increasing edge length. Figure 2b displays the observed evolution of the m = 1 FP mode dephasing time with the edge length. The longest dephasing time of ∼11.5 fs is observed for the 2150 nm NT. While limited to only the smallest NTs due to computational resources, numerical calculations (inset) are in good agreement as evaluated by the slope of the lines interpolated through the numerical (0.00292 fs·nm^{-1}) and experimental (0.00379 fs·nm^{-1}) data. Discrepancy between experimental and calculated dephasing times can be attributed to substrate effects, variation in NT thickness, and edge-roundness, which were not modeled numerically.

To further investigate the multipolar FP character of the NT, we experimentally measure and numerically simulate the EEL spectral responses of a 680 nm gold NT as a function of the electron beam impact parameter. As shown in the schematic of Figure 3, we collect spectra as a function of the

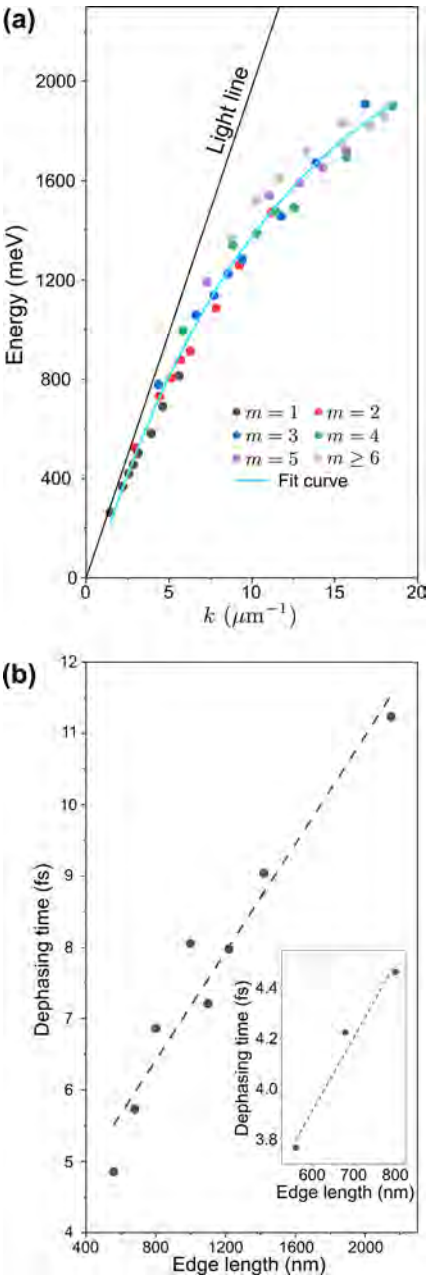

Figure 2. Experimentally measured (a) energy-momentum dispersion for the m = 1−7 FP modes and (b) the associated dephasing times for the dipolar (m = 1) FP mode of individual gold NTs of different edge lengths. The dashed line is a linear fit for a visual aid. Numerically calculated dephasing times for the NT's m = 1 FP mode versus edge length are shown in the inset.

impact parameter along a line varying from 100 nm outside of the NT corner ($-d/2$ − 100 nm) to 100 nm outside of the NT edge ($d/2$ + 100 nm). In Figure 3a,b, the experimentally measured and simulated EEL probabilities as a function of impact parameter are plotted for regions within the NT, respectively. Similarly, for regions outside of the NT, the experimentally measured and simulated EEL probabilities are shown in Figure 3c,d, respectively. All EEL probabilities are individually normalized with respect to the maximum value.

In Figure 3, the four lowest order multipoles are evident by the strong regions of EEL probability, each of which is excited when the electron beam impact parameter is close to the NT

https://doi.org/10.1021/acs.jpcc.3c00753
J. Phys. Chem. C 2023, 127, 6777−6784

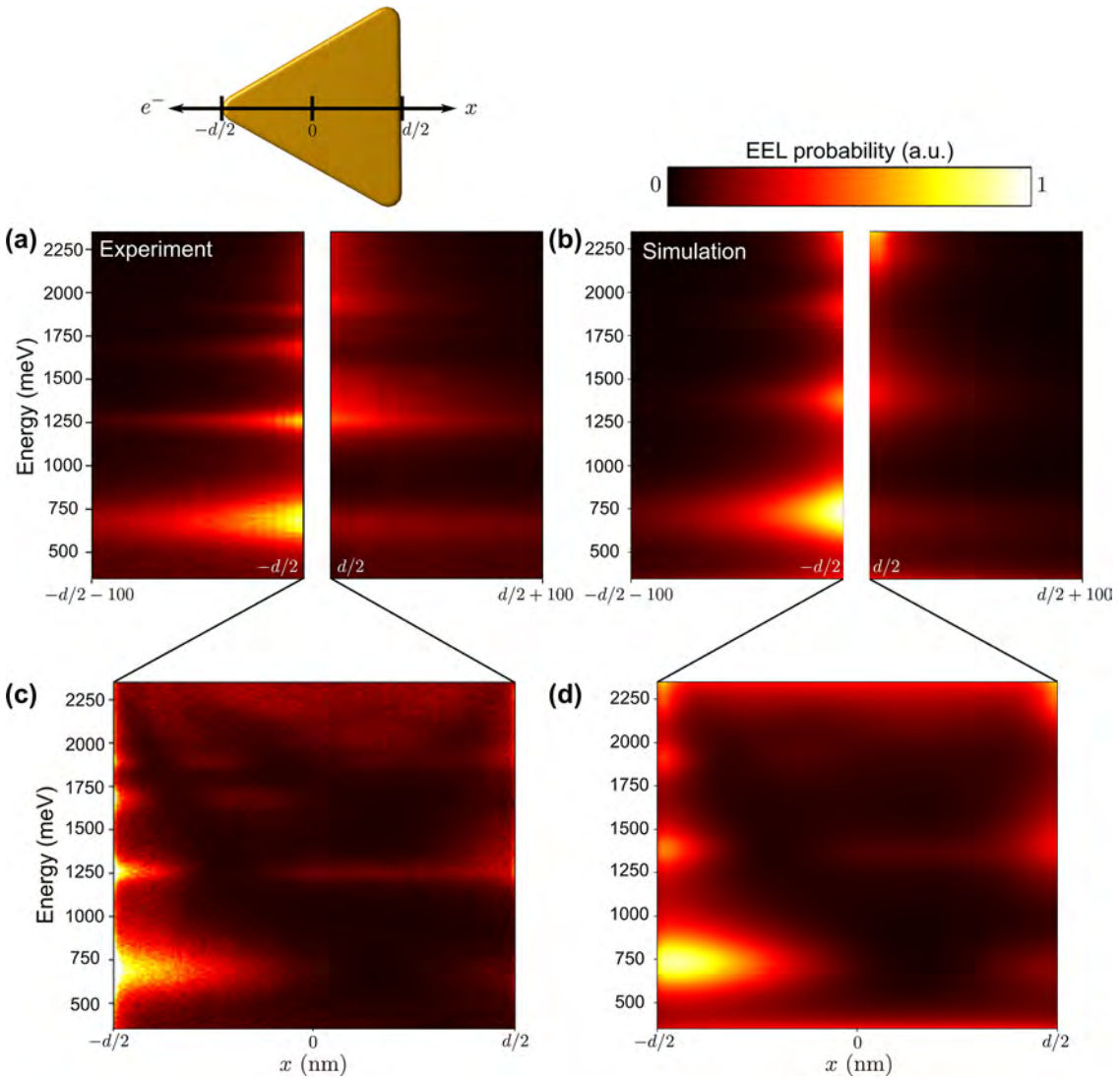

Figure 3. Comparison of experimental and numerical NT spectrum images. The schematic depicts the scanning of the electron beam across a 680 nm NT of height d = 590 nm and thickness 70 nm to obtain spectra at each impact parameter. (a,b) The experimental and simulated EEL probability as a function of impact parameter for regions within the NT, respectively. (c,d) The experimental and simulated EEL probability as a function of the impact parameter for regions outside of the NT, respectively. All EEL probabilities are individually normalized with respect to the maximum value.

corner ($-d/2$). Due to selection rules (see Figure 1a), odd numbered multipoles are not excited when the impact parameter biases the edge of the NT ($d/2$). As expected, the presence of a substrate red-shifts the experimentally measured resonances relative to the simulated values,[57] which were calculated in a background refractive index of unity. For regions inside of the NT (Figure 3a,b), the EEL probability of certain multipoles (at a fixed energy) exhibits strong spatial variation as a result of the electron beam probing different spatial regions of the FP mode profile.

Therefore, similar to gold nanowires,[15] nanotriangles host high-quality IR plasmons, which can be easily tuned to cover a wide spectral window by changing the geometric parameters. However, a direct comparison of their near-field enhancement factors has been lacking in the IR region. Therefore, we compare the simulated enhancement factors of these two nanostructures under optical excitation as a function of the m = 1 resonance energy, as shown in Figure 4. The NT edge length is varied from 280 to 680 nm (right to left in Figure 4) in

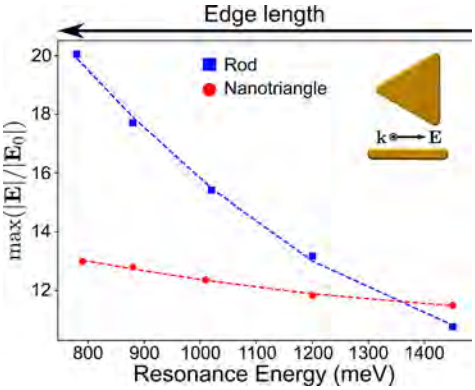

Figure 4. Comparison of the electric field enhancement of the m = 1 FP mode for rods and NTs of varying resonance energies. The inset depicts the plane wave excitation geometry used. The length of the rods was tuned to overlap spectrally with the resonance energy of the corresponding NT, while the thickness was fixed at 70 nm.

https://doi.org/10.1021/acs.jpcc.3c00753
J. Phys. Chem. C 2023, 127, 6777−6784

increments of 100 nm. Computed field enhancement data from resonant nanorods of length 250, 330, 420, 515, and 615 nm are added for comparison. The thickness of all nanorods and NTs is 70 nm. Figure S9 displays the computed electric field map of the 680 nm NT and 615 nm nanorod for comparison.

As shown in the inset of Figure 4, the wavevector **k** of the exciting plane wave is oriented perpendicular to the NT plane and the nanorod axis. To excite the m = 1 FP mode in both structures, the electric field is polarized horizontally. The maximum value of the electric field magnitude normalized to the incident electric field, max($|\mathbf{E}|/|\mathbf{E}_0|$), is calculated in the plane 5 nm above the surface of the structures (along the direction **k**). For the m = 1 FP mode of rods and NTs, the location of the strongest field enhancement is at the tip. The blue and red dashed lines in Figure 4 represent quadratic fits to the rod and NT data, respectively. As evident in Figure 4, smaller NTs with resonance energies $\lesssim$ 1375 meV have larger electric field enhancement factors compared to rods of comparable resonance energy. This is likely due to charge confinement in NTs of a smaller edge length, which would lead to greater field enhancement.

4. CONCLUSION

In summary, we have characterized the plasmonic FP responses of a set of individual gold NT plasmons over a broad IR spectral window (200−1500 meV) using monochromated STEM-EELS. We have found that the NT mode energies can be tuned by controlling the NT edge length, as the FP resonance frequencies progressively red-shift with an increasing edge length. We have measured the dispersion for different edge lengths and found that synthesized gold NTs sustain nonradiative surface plasmon polaritons. Line width analysis reveals that dipolar FP resonances become spectrally narrower with an increasing edge length, thus providing a means to engineer plasmon lifetimes for efficient IR energy harvesting. The experimentally observed spectral and spatial extent of the different multipolar plasmonic FP modes, both inside and outside of the NTs has been interpreted through numerical simulations of the electron probe. The latter were also used to calculate the electric field enhancement factors for the NT and compare them to the nanorod as a function of the edge length which reveals that the nanorod geometry shows higher enhancement factors in the IR region while the NT shape shows higher enhancement in the visible region. Taken together, these results provide insight into the design of noble metal plasmonic nanostructures capable of efficiently harvesting electromagnetic radiation for next-generation catalytic, solar-energy harvesting, and sensing based applications spanning across the broad infrared spectral domain.

■ ASSOCIATED CONTENT

Supporting Information

The Supporting Information is available free of charge at https://pubs.acs.org/doi/10.1021/acs.jpcc.3c00753.

Thickness measurement; simulated EELS spectrum profiles and EELS intensity maps; plasmon line width analysis and Lorentzian fitting; and simulated electric-field maps (PDF)

■ AUTHOR INFORMATION

Corresponding Authors

David J. Masiello − *Department of Chemistry, University of Washington, Seattle, Washington 98195, United States;* orcid.org/0000-0002-1187-0920; Email: masiello@uw.edu

Jon P. Camden − *Department of Chemistry and Biochemistry, University of Notre Dame, Notre Dame, Indiana 46556, United States;* orcid.org/0000-0002-6179-2692; Email: jon.camden@nd.edu

Authors

Vishal Kumar − *Department of Chemistry and Biochemistry, University of Notre Dame, Notre Dame, Indiana 46556, United States*

Andrew W. Rossi − *Department of Chemistry, University of Washington, Seattle, Washington 98195, United States*

Zachary R. Lawson − *College of Engineering, University of Notre Dame, Notre Dame, Indiana 46556, United States*

Robert D. Neal − *College of Engineering, University of Notre Dame, Notre Dame, Indiana 46556, United States*

Jordan A. Hachtel − *Center for Nanophase Materials Sciences, Oak Ridge National Laboratory, Oak Ridge, Tennessee 37830, United States;* orcid.org/0000-0002-9728-0920

Svetlana Neretina − *College of Engineering and Department of Chemistry and Biochemistry, University of Notre Dame, Notre Dame, Indiana 46556, United States;* orcid.org/0000-0002-6889-4384

Complete contact information is available at: https://pubs.acs.org/10.1021/acs.jpcc.3c00753

Notes

Any opinions, findings, and conclusions or recommendations expressed in this material are those of the authors and do not necessarily reflect the views of the United States Air Force. The authors declare no competing financial interest.

■ ACKNOWLEDGMENTS

This material is based upon work supported by the Air Force Office of Scientific Research under Award FA9550-21-1-0282 (V.K., A.W.R, D.J.M., J.P.C.). The NT synthesis work is supported by an award to S.N. from the National Science Foundation, Division of Chemistry, Macromolecular, Supramolecular, and Nanochemistry (MSN) Program under Grant No. CHE2107728 (Z.R.L., R.D.N., S.N.). STEM-EELS experiments were conducted at the Center for Nanophase Materials Sciences, which is a DOE Office of Science User Facility (J.A.H.). This research was conducted, in part, using instrumentation within ORNL's Materials Characterization Core provided by UT-Battelle, LLC, under Contract No. DE-AC05-00OR22725 with the DOE, and sponsored by the Laboratory Directed Research and Development Program of Oak Ridge National Laboratory, managed by UT-Battelle, LLC, for the U.S. Department of Energy.

■ REFERENCES

(1) Schuller, J. A.; Barnard, E. S.; Cai, W.; Jun, Y. C.; White, J. S.; Brongersma, M. L. Plasmonics for extreme light concentration and manipulation. *Nat. Mater.* **2010**, *9*, 193−204.

(2) Yu, H.; Peng, Y.; Yang, Y.; Li, Z.-Y. Plasmon-enhanced light−matter interactions and applications. *npj Comput. Mater.* **2019**, *5*, 45.

(3) Atwater, H. A.; Polman, A. Plasmonics for improved photovoltaic devices. *Nat. Mater.* **2010**, *9*, 205−213.

(4) Kumar, V.; Nisika, N.; Kumar, M. Modified absorption and emission properties leading to intriguing applications in plasmonic−excitonic nanostructures. *Adv. Opt. Mater.* **2021**, *9*, 2001150.
(5) Gelle, A.; Jin, T.; de la Garza, L.; Price, G. D.; Besteiro, L. V.; Moores, A. Applications of plasmon-enhanced nanocatalysis to organic transformations. *Chem. Rev.* **2020**, *120*, 986−1041.
(6) Olafsson, A.; Busche, J. A.; Araujo, J. J.; Maiti, A.; Idrobo, J. C.; Gamelin, D. R.; Masiello, D. J.; Camden, J. P. Electron beam infrared nano-ellipsometry of individual indium tin oxide nanocrystals. *Nano Lett.* **2020**, *20*, 7987−7994.
(7) Agrawal, A.; Cho, S. H.; Zandi, O.; Ghosh, S.; Johns, R. W.; Milliron, D. J. Localized surface plasmon resonance in semiconductor nanocrystals. *Chem. Rev.* **2018**, *118*, 3121−3207.
(8) Baiz, C. R.; B lasiak, B.; Bredenbeck, J.; Cho, M.; Choi, J.-H.; Corcelli, S. A.; Dijkstra, A. G.; Feng, C.-J.; Garrett-Roe, S.; Ge, N.-H.; et al. Vibrational spectroscopic map, vibrational spectroscopy, and intermolecular interaction. *Chem. Rev.* **2020**, *120*, 7152−7218.
(9) Arora, A. K.; Rajalakshmi, M.; Ravindran, T.; Sivasubramanian, V. Raman spectroscopy of optical phonon confinement in nanostructured materials. *J. Raman Spectrosc.* **2007**, *38*, 604−617.
(10) Konečná, A.; Li, J.; Edgar, J. H.; García de Abajo, F. J.; Hachtel, J. A. Revealing nanoscale confinement effects on hyperbolic phonon polaritons with an electron beam. *Small* **2021**, *17*, 2103404.
(11) Rodrigo, D.; Limaj, O.; Janner, D.; Etezadi, D.; García de Abajo, F. J.; Pruneri, V.; Altug, H. Mid-infrared plasmonic biosensing with graphene. *Science* **2015**, *349*, 165−168.
(12) Neubrech, F.; Huck, C.; Weber, K.; Pucci, A.; Giessen, H. Surface-enhanced infrared spectroscopy using resonant nanoantennas. *Chem. Rev.* **2017**, *117*, 5110−5145.
(13) Smith, K. C.; Olafsson, A.; Hu, X.; Quillin, S. C.; Idrobo, J. C.; Collette, R.; Rack, P. D.; Camden, J. P.; Masiello, D. J. Direct observation of infrared plasmonic fano antiresonances by a nanoscale electron probe. *Phys. Rev. Lett.* **2019**, *123*, 177401.
(14) Wang, T.; Li, P.; Chigrin, D. N.; Giles, A. J.; Bezares, F. J.; Glembocki, O. J.; Caldwell, J. D.; Taubner, T. Phonon-polaritonic bowtie nanoantennas: controlling infrared thermal radiation at the nanoscale. *ACS Photonics* **2017**, *4*, 1753−1760.
(15) Wu, Y.; Hu, Z.; Kong, X.-T.; Idrobo, J. C.; Nixon, A. G.; Rack, P. D.; Masiello, D. J.; Camden, J. P. Infrared plasmonics: STEM-EELS characterization of Fabry-Pérot resonance damping in gold nanowires. *Phys. Rev. B* **2020**, *101*, No. 085409.
(16) Mkhitaryan, V.; March, K.; Tseng, E. N.; Li, X.; Scarabelli, L.; Liz-Marzán, L. M.; Chen, S.-Y.; Tizei, L. H. G.; Stéphan, O.; Song, J.-M.; et al. Can copper nanostructures sustain high-quality plasmons? *Nano Lett.* **2021**, *21*, 2444−2452.
(17) Rossouw, D.; Botton, G. A. Plasmonic response of bent silver nanowires for nanophotonic subwavelength waveguiding. *Phys. Rev. Lett.* **2013**, *110*, No. 066801.
(18) Amendola, V.; Bakr, O. M.; Stellacci, F. A study of the surface plasmon resonance of silver nanoparticles by the discrete dipole approximation method: effect of shape, size, structure, and assembly. *Plasmonics* **2010**, *5*, 85−97.
(19) Ha, M.; Kim, J.-H.; You, M.; Li, Q.; Fan, C.; Nam, J.-M. Multicomponent plasmonic nanoparticles: from heterostructured nanoparticles to colloidal composite nanostructures. *Chem. Rev.* **2019**, *119*, 12208−12278.
(20) Agrawal, A.; Kriegel, I.; Milliron, D. J. Shape-dependent field enhancement and Plasmon resonance of oxide nanocrystals. *J. Phys. Chem. C* **2015**, *119*, 6227−6238.
(21) Neal, R. D.; Hughes, R. A.; Preston, A. S.; Golze, S. D.; Demille, T. B.; Neretina, S. Substrate-immobilized noble metal nanoplates: a review of their synthesis, assembly, and application. *J. Mater. Chem. C* **2021**, *9*, 12974−13012.
(22) Campos, A.; Arbouet, A.; Martin, J.; Gerard, D.; Proust, J.; Plain, J.; Kociak, M. Plasmonic breathing and edge modes in aluminum nanotriangles. *ACS Photonics* **2017**, *4*, 1257−1263.
(23) Hao, E.; Schatz, G. C. Electromagnetic fields around silver nanoparticles and dimers. *J. Chem. Phys.* **2004**, *120*, 357−366.
(24) Tanaka, Y. Y.; Shimura, T. Tridirectional polarization routing of light by a single triangular plasmonic nanoparticle. *Nano Lett.* **2017**, *17*, 3165−3170.
(25) Li, Z.; Yu, Y.; Chen, Z.; Liu, T.; Zhou, Z.-K.; Han, J.-B.; Li, J.; Jin, C.; Wang, X. Ultrafast third-order optical nonlinearity in au triangular nanoprism with strong dipole and quadrupole plasmon resonance. *J. Phys. Chem. C* **2013**, *117*, 20127−20132.
(26) Yankovich, A. B.; Munkhbat, B.; Baranov, D. G.; Cuadra, J.; Olsén, E.; Lourenço-Martins, H.; Tizei, L. H.; Kociak, M.; Olsson, E.; Shegai, T. Visualizing spatial variations of plasmon−exciton polaritons at the nanoscale using electron microscopy. *Nano Lett.* **2019**, *19*, 8171−8181.
(27) Wild, B.; Cao, L.; Sun, Y.; Khanal, B. P.; Zubarev, E. R.; Gray, S. K.; Scherer, N. F.; Pelton, M. Propagation lengths and group velocities of plasmons in chemically synthesized gold and silver nanowires. *ACS Nano* **2012**, *6*, 472−482.
(28) Khanal, B. P.; Zubarev, E. R. Purification of high aspect ratio gold nanorods: complete removal of platelets. *J. Am. Chem. Soc.* **2008**, *130*, 12634−12635.
(29) Tan, T.; Zhang, S.; Wang, J.; Zheng, Y.; Lai, H.; Liu, J.; Qin, F.; Wang, C. Resolving the stacking fault structure of silver nanoplates. *Nanoscale* **2021**, *13*, 195−205.
(30) Koh, A. L.; Fernández-Domínguez, A. I.; McComb, D. W.; Maier, S. A.; Yang, J. K. High-resolution mapping of electron-beam-excited plasmon modes in lithographically defined gold nanostructures. *Nano Lett.* **2011**, *11*, 1323−1330.
(31) Neal, R. D.; Lawson, Z. R.; Tuff, W. J.; Xu, K.; Kumar, V.; Korsa, M. T.; Zhukovskyi, M.; Rosenberger, M. R.; Adam, J.; Hachtel, J. A.; et al. Large-area periodic arrays of atomically flat single-crystal gold nanotriangles formed directly on substrate surfaces. *Small* **2022**, *18*, 2205780.
(32) Baida, H.; Billaud, P.; Marhaba, S.; Christofilos, D.; Cottancin, E.; Crut, A.; Lermé, J.; Maioli, P.; Pellarin, M.; Broyer, M.; et al. Quantitative determination of the size dependence of surface plasmon resonance damping in single Ag@ SiO2 nanoparticles. *Nano Lett.* **2009**, *9*, 3463−3469.
(33) Lee, S. A.; Link, S. Chemical interface damping of surface plasmon resonances. *Acc. Chem. Res.* **2021**, *54*, 1950−1960.
(34) Alekseeva, S.; Nedrygailov, I. I.; Langhammer, C. Single particle plasmonics for materials science and single particle catalysis. *ACS Photonics* **2019**, *6*, 1319−1330.
(35) Yao, Z.; Xu, S.; Hu, D.; Chen, X.; Dai, Q.; Liu, M. Nanoimaging and nanospectroscopy of polaritons with time resolved s-SNOM. *Adv. Opt. Mater.* **2020**, *8*, 1901042.
(36) Kumar, V.; Nisika, N.; Kumar, M. Temporal-spatial-energy resolved advance multidimensional techniques to probe photovoltaic materials from atomistic viewpoint for next-generation energy solutions. *Energy Environ. Sci.* **2021**, *14*, 4760−4802.
(37) Wu, Y.; Li, G.; Camden, J. P. Probing nanoparticle plasmons with electron energy loss spectroscopy. *Chem. Rev.* **2018**, *118*, 2994−3031.
(38) Nelayah, J.; Kociak, M.; Stéphan, O.; García de Abajo, F. J.; Tencé, M.; Henrard, L.; Taverna, D.; Pastoriza-Santos, I.; Liz-Marzán, L. M.; Colliex, C. Mapping surface plasmons on a single metallic nanoparticle. *Nat. Phys.* **2007**, *3*, 348−353.
(39) Guiton, B. S.; Iberi, V.; Li, S.; Leonard, D. N.; Parish, C. M.; Kotula, P. G.; Varela, M.; Schatz, G. C.; Pennycook, S. J.; Camden, J. P. Correlated optical measurements and plasmon mapping of silver nanorods. *Nano Lett.* **2011**, *11*, 3482−3488.
(40) Bigelow, N. W.; Vaschillo, A.; Iberi, V.; Camden, J. P.; Masiello, D. J. Characterization of the electron-and photon-driven plasmonic excitations of metal nanorods. *ACS Nano* **2012**, *6*, 7497−7504.
(41) Krivanek, O. L.; Lovejoy, T. C.; Dellby, N.; Aoki, T.; Carpenter, R.; Rez, P.; Soignard, E.; Zhu, J.; Batson, P. E.; Lagos, M. J.; et al. Vibrational spectroscopy in the electron microscope. *Nature* **2014**, *514*, 209−212.
(42) Kumar, V.; Camden, J. P. Imaging vibrational excitations in the electron microscope. *J. Phys. Chem. C* **2022**, *126*, 16919−16927.

https://doi.org/10.1021/acs.jpcc.3c00753
J. Phys. Chem. C 2023, 127, 6777−6784

(43) Venkatraman, K.; Levin, B. D.; March, K.; Rez, P.; Crozier, P. A. Vibrational spectroscopy at atomic resolution with electron impact scattering. *Nat. Phys.* **2019**, *15*, 1237−1241.
(44) Hachtel, J. A.; Huang, J.; Popovs, I.; Jansone-Popova, S.; Keum, J. K.; Jakowski, J.; Lovejoy, T. C.; Dellby, N.; Krivanek, O. L.; Idrobo, J. C. Identification of site-specific isotopic labels by vibrational spectroscopy in the electron microscope. *Science* **2019**, *363*, 525−528.
(45) Hage, F.; Radtke, G.; Kepaptsoglou, D.; Lazzeri, M.; Ramasse, Q. Single-atom vibrational spectroscopy in the scanning transmission electron microscope. *Science* **2020**, *367*, 1124−1127.
(46) Golze, S. D.; Hughes, R. A.; Rouvimov, S.; Neal, R. D.; Demille, T. B.; Neretina, S. Plasmon-mediated synthesis of periodic arrays of gold nanoplates using substrateimmobilized seeds lined with planar defects. *Nano Lett.* **2019**, *19*, 5653−5660.
(47) Li, G.; Cherqui, C.; Bigelow, N. W.; Duscher, G.; Straney, P. J.; Millstone, J. E.; Masiello, D. J.; Camden, J. P. Spatially mapping energy transfer from single plasmonic particles to semiconductor substrates via STEM/EELS. *Nano Lett.* **2015**, *15*, 3465−3471.
(48) Farzinpour, P.; Sundar, A.; Gilroy, K.; Eskin, Z.; Hughes, R.; Neretina, S. Altering the dewetting characteristics of ultrathin gold and silver films using a sacrificial antimony layer. *Nanotechnology* **2012**, *23*, 495604.
(49) Hachtel, J. A.; Lupini, A. R.; Idrobo, J. C. Exploring the capabilities of monochromated electron energy loss spectroscopy in the infrared regime. *Sci. Rep.* **2018**, *8*, 5637.
(50) Malis, T.; Cheng, S.; Egerton, R. EELS log-ratio technique for specimen-thickness measurement in the TEM. *J. Electron Micr. Technol.* **1988**, *8*, 193−200.
(51) Hohenester, U.; Trügler, A. MNPBEM−A Matlab toolbox for the simulation of plasmonic nanoparticles. *Comput. Phys. Commun.* **2012**, *183*, 370−381.
(52) Olmon, R. L.; Slovick, B.; Johnson, T. W.; Shelton, D.; Oh, S.-H.; Boreman, G. D.; Raschke, M. B. Optical dielectric function of gold. *Phys. Rev. B* **2012**, *86*, 235147.
(53) Rossouw, D.; Couillard, M.; Vickery, J.; Kumacheva, E.; Botton, G. Multipolar plasmonic resonances in silver nanowire antennas imaged with a subnanometer electron probe. *Nano Lett.* **2011**, *11*, 1499−1504.
(54) Plotkin-Swing, B.; Corbin, G. J.; De Carlo, S.; Dellby, N.; Hoermann, C.; Hoffman, M. V.; Lovejoy, T. C.; Meyer, C. E.; Mittelberger, A.; Pantelic, R.; et al. Hybrid pixel direct detector for electron energy loss spectroscopy. *Ultramicroscopy* **2020**, *217*, 113067.
(55) Dastmalchi, B.; Tassin, P.; Koschny, T.; Soukoulis, C. M. A new perspective on plasmonics: confinement and propagation length of surface plasmons for different materials and geometries. *Adv. Opt. Mater.* **2016**, *4*, 177−184.
(56) Polman, A.; Kociak, M.; García de Abajo, F. J. Electron-beam spectroscopy for nanophotonics. *Nat. Mater.* **2019**, *18*, 1158−1171.
(57) Olafsson, A.; Khorasani, S.; Busche, J. A.; Araujo, J. J.; Idrobo, J. C.; Gamelin, D. R.; Masiello, D. J.; Camden, J. P. Imaging infrared plasmon hybridization in doped semiconductor nanocrystal dimers. *J. Phys. Chem. Lett.* **2021**, *12*, 10270−10276.

https://doi.org/10.1021/acs.jpcc.3c00753
J. Phys. Chem. C 2023, 127, 6777−6784